



# Engineering of ultrasound contracts agents-focused cabazitaxel-loaded microbubbles nanomaterials induces cell proliferation and enhancing apoptosis in cancer cells

Huilin Liu<sup>1</sup> · Lianjie Bai<sup>1</sup> · Zihe Chen<sup>2</sup> · Xing Li<sup>1</sup> · Ying Wang<sup>1</sup> · Weiyang Lv<sup>1</sup>

Received: 19 November 2021 / Accepted: 16 January 2022 / Published online: 28 February 2022  
© King Abdulaziz City for Science and Technology 2022

## Abstract

Tumour-induced sentinel lymph node diagnosis and metastatic therapeutic techniques are limited by current strategies nowadays. Herein, we combined iron oxide nanomaterials with chemotherapy drugs in poly(lactic-co-glycolic acid) multifunctional microbubbles (MMBs) to develop and visualize tumour lymph node treatment. Fabrication and loading of perfluorocarbon gas-filled PLGA microbubbles with co-encapsulated cabazitaxel (CTX) and Fe<sub>3</sub>O<sub>4</sub> nanomaterials were accomplished. Ultrasound (US) imaging enhancement and US-induced drug delivery have been investigated in vitro and in vivo to improve the outcomes. The MMBs had a mean size of 881.45 ± 70.19 nm, with a narrow size dispersion and a smooth surface. It was also shown that the amount of Fe<sub>3</sub>O<sub>4</sub> nanomaterials in the MBs did not affect the CTX drug loading efficiency or encapsulation. Our outcomes showed that these MMBs could improve ultrasound imaging in vitro and in vivo and improve tumour lymph node signals. Biomarkers of tumour proliferation profile and micro blood/lymphatic vessel density were used to assess the anti-tumour efficacy of MMBs-mediated chemotherapy in vivo. These markers were consistently lower after MMBs + sonication treatment than controls. The tumour cell apoptosis index was shown to be highest following MMBs plus sonication treatment, which is in line with this finding. A cabazitaxel-loaded PLGA-Fe<sub>3</sub>O<sub>4</sub> nanomaterials therapeutic and diagnostic agent for low-frequency US-triggered US imaging of the lymph node metastasis has been developed successfully. It may provide an approach for the chemotherapy and imaging of primary metastasis tumours.

**Keywords** Cabazitaxel · Iron oxide · Microbubbles · US imaging · US-triggered therapy

## Introduction

Immunity and tissue fluid homeostasis are both critical functions of the lymphatic system. Extracellular fluids, including tissue waste and antigens, are collected by early lymphatic channels under normal physiological conditions (Schreuder et al. 2020; Eide et al. 2018; Lee et al. 2019). These fluids and immune cells are assembled to form lymph, which is then carried to regional lymph nodes (LNs), wherein adaptive immune response can be activated by lymphatic

veins that collect lymph (Najibi and Mooney 2020). Lymph returns to the circulation after being monitored by LNs and cleared. Lymphatic arteries and LNs that drain them can be damaged by infection, chronic inflammation, and malignancy. Cancer cells can also spread through the lymphatic system and settle in the LNs that drain them (Huang et al. 2021). As a result, the immune system of metastatic LNs is repressed. Recent research summarizes that cancer manipulates the lymphatic system to produce lymph node metastases, escape the immune response, and spread to other organs (Ding et al. 2021). We also address future clinical opportunities to target lymph node metastases (Steiner et al. 2018; Schudel et al. 2020).

Nano-biotechnology, significant organic molecule chemistry, and polymeric conjugation technique improvements have made designing drugs for lymphatic system delivery (Lv et al. 2020, 2019; Gong et al. 2021; Chen et al. 2021). In the last era, lymphatic administration of drug-loaded polymer nano-/microparticles has been widely studied to enhance

✉ Huilin Liu  
huilinliu34@yahoo.com

<sup>1</sup> Department of Ultrasound, The Second Affiliated Hospital of Qiqihar Medical University, No. 333 Bukui North Street, Jianhua District, Qiqihar 161006, China

<sup>2</sup> Qiqihar Medical University, Jianhua District, Qiqihar 161006, China

lymphatic target and metastasis tumour suppression (Zhang et al. 2019a). A gelatin matrix combined with fluorescently tagged PLGA-rhodamine microspheres and paclitaxel-loaded PLGA was studied by Liu et al. (Liu et al. 2019a). For lymphatic targeting in healthy and cancer-bearing rats following intraperitoneal and intrapleural implantation. They discovered that intraperitoneal and intrapleural injection of PLGA–rhodamine microspheres caused the localized and distant LNs to take up the microspheres spontaneously (Shi et al. 2018). PLGA nanomaterials were inoculated into the dorsal side footpads of the rats', one made of PP nanomaterials and the other of PLGA–PMA: PLGA–COOH, PC nanomaterials (Liu et al. 2019a). A correlation was shown between PP nanoparticles lymphatic absorption and retention and particle size and hydrophobicity, whereas the anionic charge of PC nanomaterials was directly connected to these outcomes. Therefore, the study determined that polymeric nano- and microparticles offer tremendous potential for lymphatic drug delivery (Sanz-Ortega et al. 2019). Additionally, polymeric nano- or microparticles serve as the US contrast in LNs imagination, i.e., drug delivery methods and theranostics for therapeutic drugs. Wistar rats were injected with Technetium-99m (99mTc)-labelled PLGA nanomaterials instead of 99mTc-labelled sulphur colloid/albumin nanocolloid. According to the previous study, scintigraphic imaging of the sentinel LNs was successful (Liu et al. 2019b; Yu et al. 2020; Zukancic et al. 2020).

Nanomaterials constructed of polymeric materials have shown tremendous promise in lymphatic system theranostic applications (Subarkhan and Ramesh 2016; Sonamuthu et al. 2020; Mohamed Subarkhan et al. 2016; Mohamed Kasim et al. 2018; Mohan et al. 2018; Balaji et al. 2020; Sathiya Kamatchi et al. 2020). Although there have been advances in lymphatic imaging technology, the present methods use dyes and radioactive tracers, which have poor sensitivity and resolution (Xin et al. 2017). Hence, they are widely desired to use, minimally invasive nature, widespread availability, and simple integrations with various imaging agents or medications are advantages of using an ultrasonographic contrast agent for lymph node identification (Ianni et al. 2019). Furthermore, ultrasonic irradiation has the potential to initiate drug release efficiently. For pre- and intraoperative lymph node localization, including ultrasonographically assisted core needle lymph node biopsy, our group recently developed an imaging agent comprising PLGA microbubbles (Li et al. 2018). According to previous studies, subareolar perfluorobutane microbubbles contrast-enhanced ultrasonography had a poorer detection rate of sentinel LNs than  $\gamma$ -detection (Devulapally et al. 2018).

Microbubbles containing superparamagnetic iron oxide (SPIO) nanomaterials outperformed perfluorocarbon gas-incorporated microbubbles without the inclusion of SPIO in terms of US imaging contrast and a remarkable

backscattering signal (Xu et al. 2017). Using  $\text{Fe}_3\text{O}_4$  nanomaterials incorporated in ultrasonographic microbubbles as potential US contrast agents for lymph ultrasonography, we hypothesized that the detection rate of LNs could be improved by using  $\text{Fe}_3\text{O}_4$  nanomaterials. This investigation aimed to establish dual-functional theranostics agents that contained perfluorocarbon gas, cabazitaxel, and  $\text{Fe}_3\text{O}_4$  nanomaterials for lymph node US imaging and the release of in situ drugs for lymph node metastases therapy using low-frequency ultrasound imaging and ultrasound-triggered in situ drug release.

## Experimental section

### Preparation of MMBs

The MMBs were constructed by slightly altering a process described by Chen et al. (Chen et al. 2019). As an outline, a stirred mixture of the  $\text{OA@Fe}_3\text{O}_4$ -NMs suspension (32 mg of  $\text{Fe}/\text{mL}$ ) was added to the PLGA organic solution (150 mg of PLGA in 2.5 mL MC) at varying concentrations. This was followed by adding 10 mg of CTX to 200  $\mu\text{L}$  of de-ionized water and the emulsification of the mixture by sonication for 40 s with 50 mg/mL of CTX solution. We removed all the formulation's free  $\text{Fe}_3\text{O}_4$  nanomaterials by employing the magnetic isolation method. A cold 5% PVA solution was then added to the original emulsions and homogenized at 9500 rpm for 5 min. To eradicate the organic solvents, the prepared double emulsion was incubated with 50 mL of a 0.3% w/v PVA solution overnight with magnetically stirred at RT. It was centrifuged and then rinsed with de-ionized water to remove any remaining debris. Three times, the centrifugation and washing steps were carried out in sequence. Finally, the microspheres were washed, dried, and loaded with perfluorocarbon gas before being frozen at 4 °C for later use. The  $\text{OA-Fe}_3\text{O}_4$ -NMs solution and CTX solution were omitted from the preparation of free MBs.

### Determination of CTX loading

UV–Vis spectrophotometry was used to measure the quantity of CTX retrieved from washed supernatants during fabrication by measuring the excitation wavelength, excitation 235 nm, at which the encapsulation efficiency and drug loading were assessed thrice. It was determined that the drug payload was proportional to the difference between the total weight of CTX and the response rate. After that, previous methods for calculating drug encapsulation and loading efficiency have been used (Zhang et al. 2019b; Wang et al. 2018; Kumar et al. 2020).

## In vitro CTX release

In vitro sonication experiments were carried out to determine how CTX released in the sound field will perform. Sonication was carried out using the same experimental settings as our earlier investigations on in vitro cell gene transfection. MWCO: 10,000 Da dialysis bags were filled with MMBs ( $\text{Fe}_3\text{O}_4 = 185.45 \mu\text{g/mL}$ ) and placed in a 1X PBS (25 mL) reservoir with stirring at 200 rpm at 37 °C. Dialysate (1 mL) was taken from the samples at regular intervals and held at 21 °C for further analysis. Fresh 1X PBS (1 mL) was introduced into the system after each sample period to maintain a constant reservoir volume. UV–Vis spectrophotometry was used to quantify the amount of CTX present in each sample. After that, the accumulative CTX ratios were calculated over time (Shen et al. 2020).

## Examination of in vitro US imaging

A custom mould with a depth of 2 cm and three 1 cm holes in the middle was used for in vitro US imaging examination (Price 2018). The agarose in the water used to make the moulds was 1% agarose. Ultrasound pictures were obtained by inserting de-ionized water and de-gassed, free MBs, and MMBs with various concentrations of  $\text{Fe}_3\text{O}_4$  nanomaterials into the mould's perforations. The Philips iU22 scanner's ultrasonic imaging system used a transmitter and a receiver, utilizing a 7.5 MHz US transducer. US imaging was captured using the same settings (Mechanical Index, gain = 10 dB and MI = 0.1). The experiments were performed thrice in total to ensure reproducibility and quality assurance.

## US imaging of rabbit in vivo tumour LNs model

Twelve rabbits (equivalent to 24 LNs tumours) were examined with US imaging two weeks following tumour inoculation. Sixty-four cancer LNs were randomly assigned to 3 groups ( $n = 8$ ; tumour LNs in every group). MMBs (at  $[\text{Fe}_3\text{O}_4] = 185.45 \mu\text{g/mL}$ ) were injected into one group. Another group received only the purified MBs as an injection. In being assured that the sterile saline had no effect, the third group of animals was controlled. Samples containing MMBs and free MBs had similar concentrations. Ketamine hydrochloride (0.65 mg/mL) was injected intramuscularly into all rabbits to induce sedation. A facemask with 0.5–2% isoflurane was utilized throughout the trial to keep the anaesthetic effect (Prat et al. 1995; Zhu 2020; Wang et al. 2015).

Utilizing the S9-3 probe, contrast-enhanced harmonic pictures of the US were acquired using a linear probe transmitting and receiving centre frequencies of 3.5 and 7.0 MHz. The LNs were located using the default harmonic imaging method (MI: 0.06 and Depth: 2 cm). Group one rabbits received a 2 mL injection of MMBs into the hind footpad,

while the other two groups received the same quantity of free MMBs or sterile saline as a control. After that, up to five minutes of massage were used to encourage contrast migration into lymphatic channels and LNs after contrast agent injection. The popliteal nodes (PNs) tumour LNs were then located using contrast lymphosonography.

## Detection of iron in vivo

The rabbit was euthanized with fatal doses of pentobarbital after each in vivo US imaging investigation, and its PNs were removed. Tissue samples from all four groups were processed and embedded in paraffin to detect iron expression using the Prussian blue stain on 12 LNs placed in a 10% neutral formalin buffered solution. A total of 12 LNs were preserved in glutaraldehyde solution for TEM inspection and split into fragments of about 1 mm<sup>3</sup> in size (Zhuang et al. 2012; Berg 2006).

## LNs treatment sites

Six groups and thirty rabbits were separated ( $n = 10$ , 60 legs totals): Saline (group I), Free MMBs (group II), Free CTX (group III), PLGA-MMBs without  $\text{Fe}_3\text{O}_4$  inclusion combined with the US (MMBs + US) (group IV), cabazitaxel with the US (CTX + the US) (group V), and MMBs combined with the US (MMBs + the US) (group VI). The saline group received sodium chloride (4 mL) injected into the hind footpads under lidocaine anaesthesia; the MMBs group received diluted MBs (1 mL) containing CTX (2 mg) injected slowly into 4 mL; the CTX group received 2 mg of CTX injected; the CTX + US group received 2 mg of CTX injected and applied US irradiation; on the first, third, and fifth days, three different treatments were administered.

## Histological assessment

Thirty rabbits' tumour LNs were removed for the histological examination on the seventh day after the initial therapy. We used 10% neutral buffered formalin to fix all of the excised LNs from the rabbit tumours. They were then treated as usual and embedded in paraffin. Using haematoxylin and eosin stains on tissue sections, histopathologists examined the condition of the tissues. Immunohistochemical labelling with antibodies against the proliferating cell nuclear antigen (PCNA) evaluated tumour cell proliferation. Using the TdT-mediated dUTP nick end labelling (TUNEL test) approach, the levels of apoptosis in these tissue slices were also examined. Tissue sections were stained with anti-CD34 and anti-lymphatic vessel endothelial hyaluronan receptor (LYVE)-1 antibodies to evaluate blood and lymphatic vessels' density. LYVE-1 indicates lymphatic endothelial cells, whereas CD34 markers indicate blood vessel endothelial

cells. A microscope identified the expression of the nuclear antigen protein in proliferating cells, apoptosis expression, blood vessels' density, and the density of lymphatic vessels (CKX41). The number of positive cells was collected semi-quantitatively by having blind observers count the number of positively stained cells from at least five randomly selected high-power fields (around 400 magnifications each). Proliferating (PI) and apoptotic (AI) were calculated from at least five randomly selected high-power fields using tumour cell staining ratios. The vascular density locations with the high density were preferred to measure blood vessel density and lymphatic vessel density. When calculating lymphatic vessel density, researchers counted all LYVE-1-positive vessels in addition to the CD34-positive to consider each stained lumen to be a separate, countable vessel (Kato et al. 2005; Ohtani and Ohtani 2008; Koukourakis et al. 2005).

### Statistical analysis

All experimental data are shown as mean  $\pm$  standard deviation, and differences between two groups were analysed by GraphPad Prism 8 software via the Student's *t* test (\*\* $p < 0.01$ ).

## Result and discussion

### Fabrication and characterizations of MMBs

In Fig. 1, cabazitaxel-loaded MMBs are delivered into LNs and released under control by low-intensity ultrasound. As a result, the size distributions of MBs were in the 800–900 nm region, and the polydispersity index was 0.812 (mean diameter:  $872.61 \pm 7.46$  nm). There were  $881.45 \pm 70.19$  nm PLGA MBs with a mean diameter of 882.30 nm and an average PDI

of 0.623. In the polymer shell, the addition of  $\text{Fe}_3\text{O}_4$  and CTX had no significant effect on MMBs size distributions, according to these findings. AAS measured the concentration of  $\text{Fe}_3\text{O}_4$  nanomaterials encapsulated in microbubbles as  $0 \pm 0$ ,  $1.52 \pm 0.06$ ,  $2.95 \pm 0.09$ ,  $5.82 \pm 0.42$ ,  $14.89 \pm 0.45$ ,  $28.49 \pm 0.75$ ,  $57.81 \pm 0.53$ , and  $186.58 \pm 2.57$   $\mu\text{g/mL}$ .

When viewed under a scanning electron microscope (SEM), the MMBs (Fig. 2A) showed an even and smooth spherical shape. The presence of hydrophobic  $\text{Fe}_3\text{O}_4$  nanomaterials in microbubble shells as demonstrated by transmission electron microscopy (TEM) improved contrast manifested as dark domains in Fig. 2B. Magnetization properties of these MMBs are by viewing in Fig. 2C. The VSM curve shows that the produced MMBs have the superparamagnetic feature, which is extremely useful for future nano-biomedical applications. There was no evidence of residual magnetism. The particle diameters were not homogeneous, with a hydrodynamic size of  $868.0 \pm 68.7$  nm, confirmed by the dynamic light scattering (DLS) techniques (Fig. 2D).

### CTX loading and encapsulation efficiency and CTX release profile

The amount of the MMBs drug carrier was assessed by the CTX loading and the CTX encapsulation efficiency (Zaki and Hafez 2012; Danafar 2018). CTX loading efficiency of these MMBs were  $5.80 \pm 0.15\%$ ,  $5.85 \pm 0.45\%$ ,  $6.25 \pm 0.30\%$ ,  $5.85 \pm 0.09\%$ ,  $6.13 \pm 0.11\%$ ,  $5.63 \pm 0.12\%$ , and  $5.98 \pm 0.18\%$ , respectively. The encapsulation efficiency of CTX in the MMBs with various concentrations of  $\text{Fe}_3\text{O}_4$  ( $1.48 \pm 0.06$ ,  $2.85 \pm 0.07$ ,  $5.78 \pm 0.35$ ,  $14.79 \pm 0.35$ ,  $27.99 \pm 0.73$ ,  $57.01 \pm 0.52$ ,  $185.45 \pm 1.56$   $\mu\text{g/mL}$ ) were  $57.99 \pm 1.59\%$ ,  $58.03 \pm 2.89\%$ ,  $61.25 \pm 3.21\%$ ,  $57.83 \pm 0.89\%$ ,  $60.98 \pm 1.23\%$ ,  $55.97 \pm 1.87\%$ , and  $60.14 \pm 2.01\%$ , respectively. From the above outcomes, we can conclude that the

**Fig. 1** Graphic representation of how cabazitaxel (CTX)-loaded MMBs are carried into the controlled release and lymph node of CTX triggered with low-intensity sonication

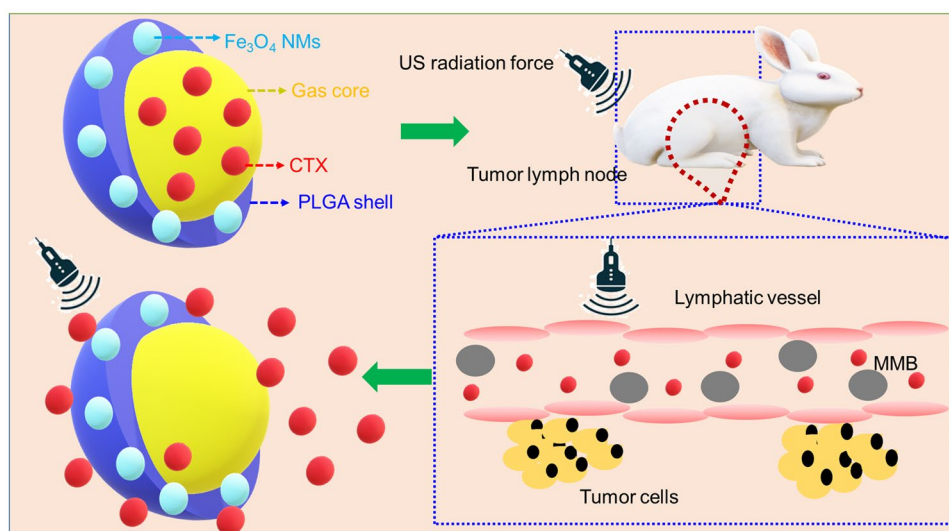
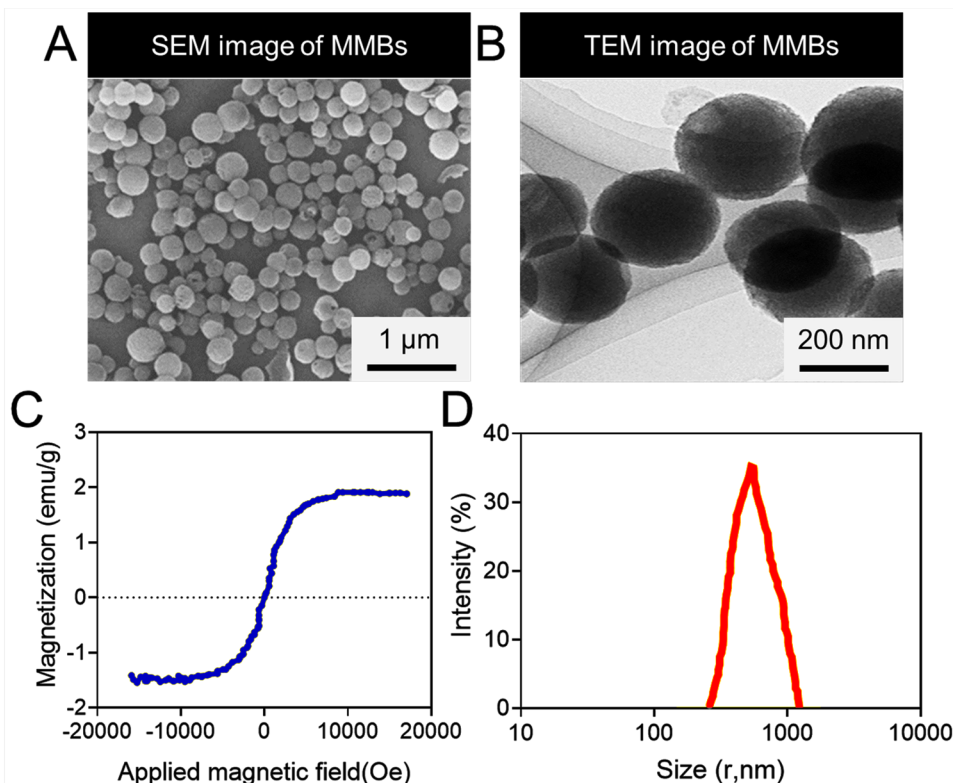


**Fig. 2** Morphological characterization of MMBs. **A** SEM image of MMBs. Scale bar 1  $\mu\text{m}$  **B** TEM image of MMBs. Scale bar 200 nm. **C** VSM curvature of MMBs. **D** Particle size distributions of MMBs by dynamic light scattering measurement (DLS)



accumulation of  $\text{Fe}_3\text{O}_4$  in the polymeric shell does not considerably impact CTX loading efficiency or encapsulation efficiency (Fig. 3A).

To determine the impact of low-frequency US sonication on CTX unloading, the release patterns of CTX from MMBs (at  $[\text{Fe}_3\text{O}_4] = 185.45 \mu\text{g/mL}$ ) were compared with and without sonication. Figure 3B depicts each release profile as a function of time, with percentages of CTX released. After

two days, 90% of the CTX was released while using sonication to release it faster than when not. However, only around 75% of the encapsulated CTX was released in the MMBs that were not sonicated. It was average roughly 5 and 10 h to release 50% of the CTX from these MMBs after sonication, but the T1/2 values for the two groups were about the same. This finding shows that the CTX-loaded MBs can be activated using the US triggered, and the CTX can be discharged

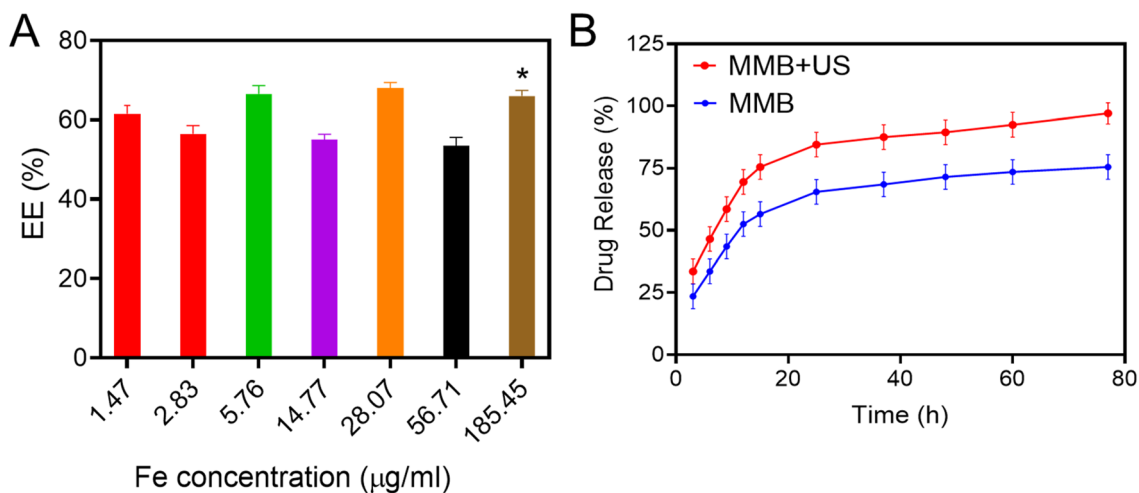


**Fig. 3** **A** The encapsulation efficiency of CTX in the MMBs with various concentrations of  $\text{Fe}_3\text{O}_4$  NMs. **B** In vitro release of CTX from MMBs without ultrasound (MMBs) and with ultrasound (MMBs + US) treatment in 1X PBS

and placed at the desired locations with the guidance of the US image.

### In vitro evaluations of MR and US imaging

MRI was used to determine the relaxation rate ( $1/T_2$ ) of MMBs and whether they could enhance magnetic resonance imaging (MRI).  $T_2$ -weighted MR images of MMBs with varying iron contents are shown in Fig. 4A. As the iron concentration increased, the images' blackness was proportional to that change (Ferrara et al. 2000; Salvo 2001; Willmann et al. 2008). A plot of the relationship between  $1/T_2$  and the iron content ( $r^2 = 0.9893/\text{mm/s}$ ) is shown in Fig. 4B. There were no significant differences in the efficacy of the MMBs as MRI contrast agents.

Additionally, the  $\text{Fe}_3\text{O}_4$  nanomaterials aided in improving US imaging. This observation has several possible explanations up until this point. According to Raisinghani et al., the multiple shell structure, or additional compounds in the shell, is responsible for this improvement in microbubble surface tension. The microbubble can significantly alter the resonance properties, amplitude of MBs volumetric oscillations, and amplitude in compression and tension. Other studies' findings suggested that the  $\text{Fe}_3\text{O}_4$  NMs and polymer shells in the shell matrix increase acoustic impedance, leading to more significant scattering signals (Liu et al. 2011).

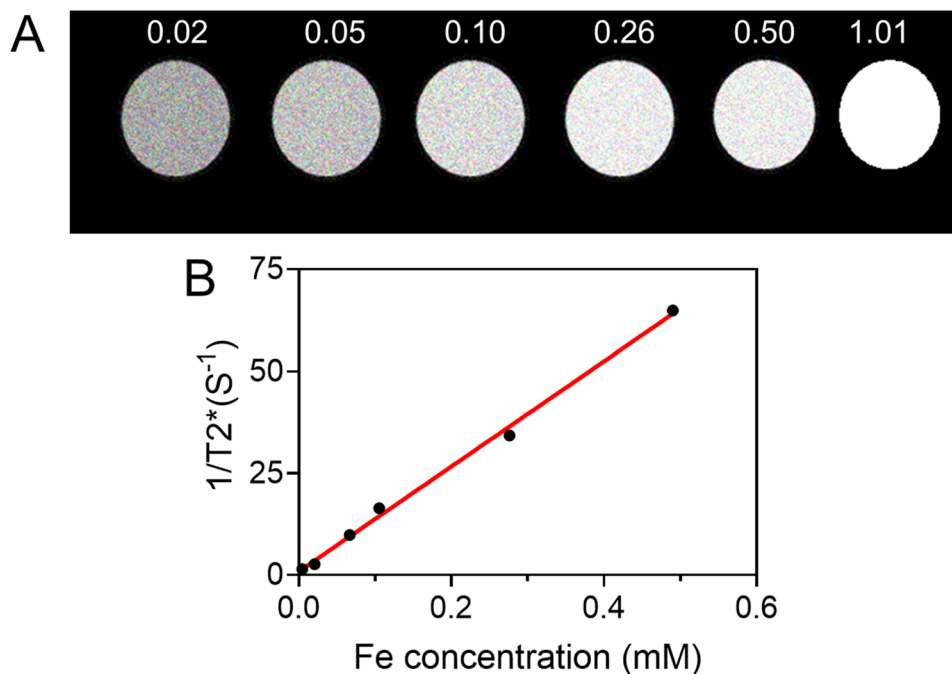
### Rabbit model tumour LNs US imaging

Further in vivo evidence of MMBs' imaging capabilities was obtained at  $[\text{Fe}_3\text{O}_4] = 185.45 \mu\text{g/mL}$ . Using contrast

lymphosonography, it was possible to tumour LNs after saline, free MBs, or MMBs were administered. A comparison of the reflectivity of PNs before and after the injection of MMBs is shown in Figure S1. In some instances, an increase in PNs could be displayed 10 s after injection. However, complete improvement was observed 15 min after injection most of the time. A boost in contrast agent transport through LNs channels and a successive raise in reflectance of afflicted PNs were attained by manipulating injection locations. A slight increment in echogenicity was observed in the saline-injected control tumour LNs throughout the imaging study (Figure S1). However, the enhanced reflectivity in the free MB-injected control tumour LNs was less than in the MMB-injected nodes (Figure S1), indicating a similar rise in echogenicity in the MBs. A comparison of US imaging enhancement data shows that MMBs outperform free MBs when using PLGA microbubbles as contrast agents, with  $\text{Fe}_3\text{O}_4$  addition having the most significant impact.

Figure 5A shows the presence of  $\text{Fe}_3\text{O}_4$  in the MMB-injected LNs. In contrast, no blue stains were demonstrated in the LNs tissues treated with free MBs, further validating the existence of MMBs in tumour LNs (Fig. 5A). Additionally, the TEM image indicated the presence of  $\text{Fe}_3\text{O}_4$  in the LNs treated with MMBs (expressed as mass black with high electrical densities), which is in line with previous findings using Prussian blue dye imaging (Fig. 5B). Tissues given with free MBs did not show an increase in electrical density (Fig. 5B). The  $\text{Fe}_3\text{O}_4$  nanomaterials were also spread in the microbubbles' shell.

**Fig. 4** MRI images visualized using a 3 T scanner in vitro. **A** MMBs with different  $\text{Fe}_3\text{O}_4$  NMs concentrations. **B** The linear fit of  $1/T_2^*$  vs Fe concentration (mM)



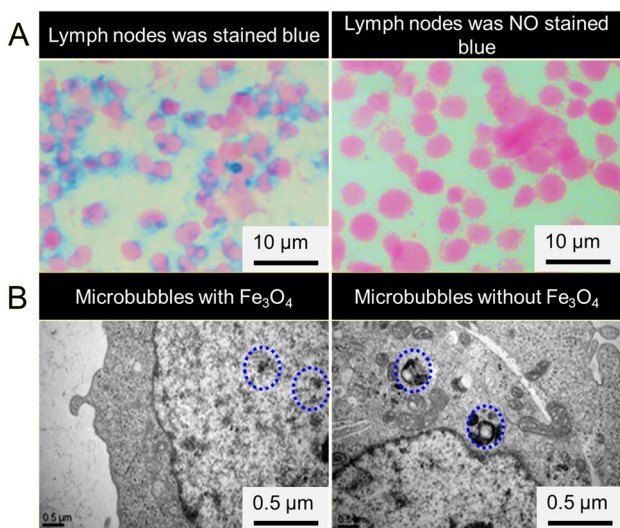


**Fig. 5** **A** The microscope images of Prussian blue dye-stained lymph nodes. The Fe in the MMB-injected lymph nodes were stained blue stain. **B** No blue stain was detected in the lymph nodes injected with MBs. Scale bar 10 µm. **C** TEM image of MMB-injected lymph nodes. **D** There were no noticeable high electronic densities in the MBs without Fe<sub>3</sub>O<sub>4</sub> NM-injected tissues. Scale bar 0.5 µm

### Histological evaluation of tumour LNs

In a tumour lymph node model, the anti-tumour activity of MMBs was investigated utilizing histological and immunohistochemical approaches. A total of 60 legs were used to divide six groups into 30 rabbits: Saline (group I), Free MMBs (group II), Free CTX (group III), PLGA-MMBs without Fe<sub>3</sub>O<sub>4</sub> inclusion combined with the US (MMBs + US) (group IV), cabazitaxel with the US (CTX + the US) (group V), and MMBs united with the US

(MMBs + the US) (group VI). Immunohistochemical labeling with antibodies against PCNA (proliferating cell nuclear antigen) was used to assess cell proliferation (Fig. 6A). Cell nuclei containing PCNA-expressed proteins show brown granules, and this was displayed in all experimental groups. Group VI (MMBs + the US) had a considerably lower proliferative index (PI) for tumour LNs than any of the other groups, according to our findings (Fig. 6B).

TUNEL assay was used to examine tissue sections for evidence of cell apoptosis (Fig. 7A). The nuclei of apoptotic cells have a dark stain on them (Witte et al. 2001; Azzali 2003; Som and Francois 2017). All groups had an increased number of apoptotic cells; however, the apoptotic index (AI) for tumour LNs in group VI (MMBs + the US) was substantially higher than the other groups (Fig. 7B). The AI did not differ significantly between saline groups and free MMBs + the US groups.

Tissue slices were stained with LYVE-1 and CD34 for determining tumour LNs micro lymphatic vessel densities (LMVD) (Fig. 8A) and micro blood vessel densities (MVD) (Fig. 9A). In one high-power (HP) field, the number of CD34-positive and LYVE-1-positive vessels was counted (Jung 2013). The most vascularly dense regions of the body were chosen for study. According to our findings, Group VI had considerably lower tumour lymph node CD34-positive vascular density than the other groups (Fig. 8B). Group VI also had significantly lower LYVE-1-positive LNs channel density in tumour LNs than the other groups. (Fig. 9B).

To summarize, we found that the tumour regressions rates correlated positively with the AI of the tumour LNs and adversely with the PI, LMVD, and MVD. Because of this, we can expect chemotherapy for tumour metastasis disorders to be considerably improved by encapsulating cabazitaxel inside polymeric MBs. The anti-tumour impact shown in

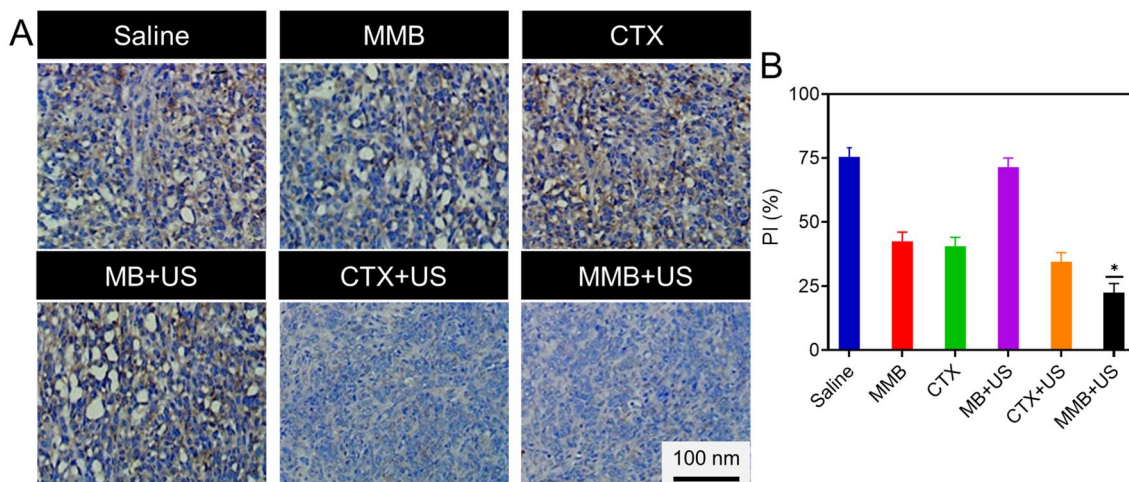


**Fig. 6** **A** Immunohistochemical PCNA staining of tumour tissues. **B** The proliferating index (PI) bar diagram of tumour cells in each group. Scale bar 100 nm

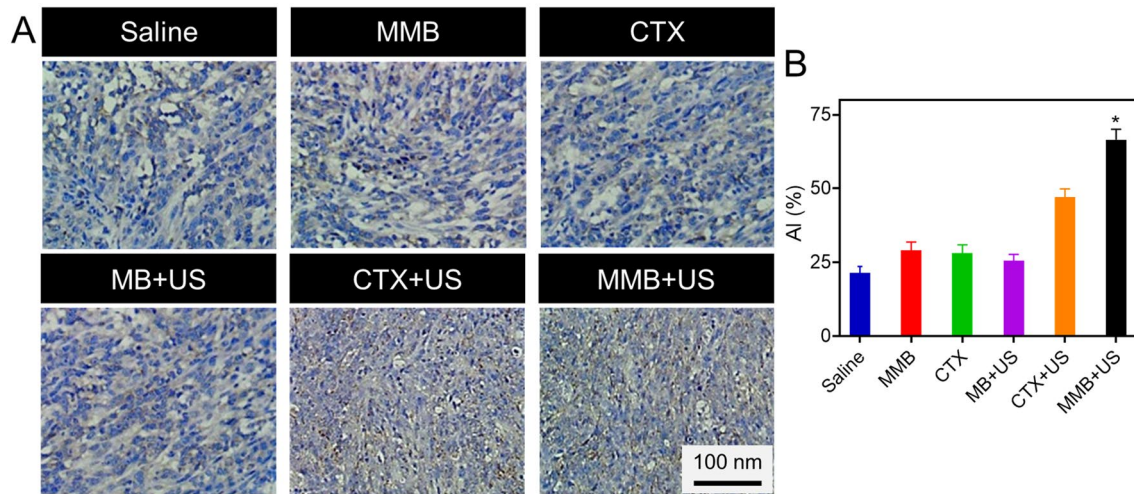


**Fig. 7** **A** Immunohistochemical TUNEL staining of tumour tissues. **B** Apoptotic index (AI) bar diagram of apoptotic cells in each group. Scale bar 100 nm

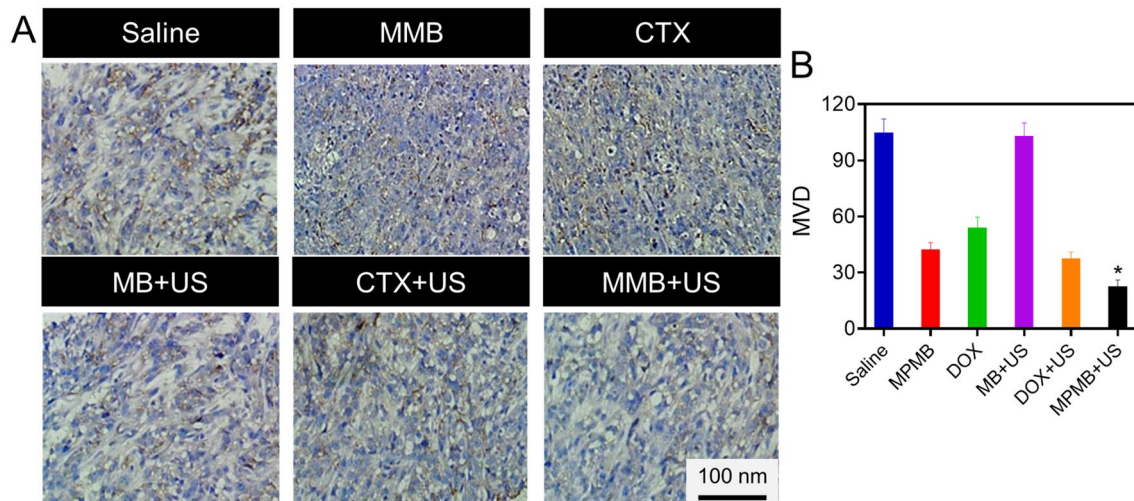


**Fig. 8** **A** Immunohistochemical CD34 staining of tumour tissues. **B** MVD bar diagram of each group. Scale bar 100 nm

the MMBs + US group could result from a complex interplay between several elements, including the drug's anticancer properties, the cavitation effect, and the possibility that US irradiation enhances the drug's anti-tumour properties.

## Conclusion

The multipurpose theranostic agent has been designed for ultrasound imaging of LNs and low-frequency ultrasound treatment to treat lymph node metastases loaded with cabazitaxel. This agent's benefits could be broadened

to include various organs and tissues, offering a new approach to imaging and treating primary tumours and their metastases as a general strategy.

**Supplementary Information** The online version contains supplementary material available at <https://doi.org/10.1007/s13204-022-02376-y>.

**Funding** This research did not receive any specific grant from funding agencies in the public, commercial, or not-for-profit sectors.

## Declarations

**Conflict of interest** The authors declare no potential conflicts of interest.



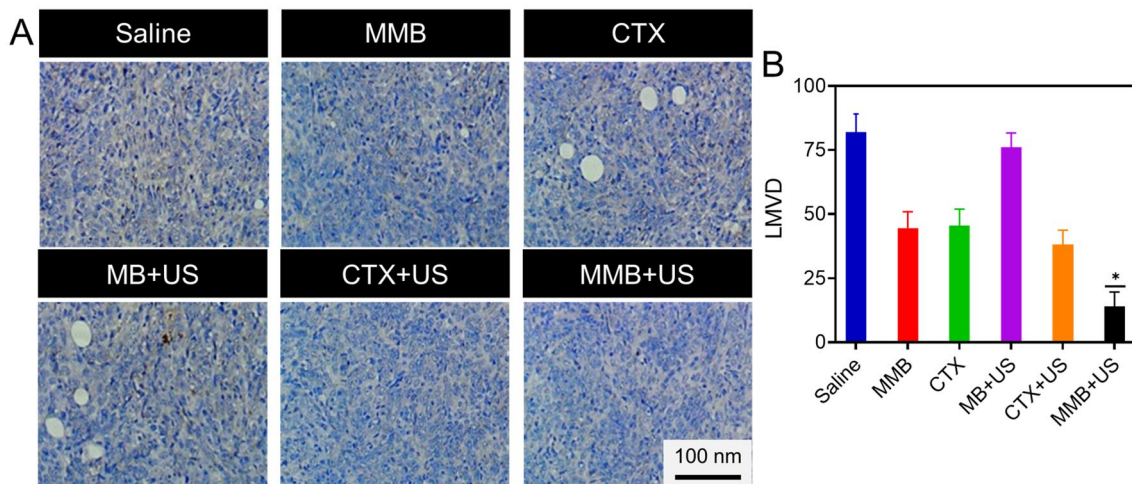


**Fig. 9** **A** Immunohistochemical LYVE-1 staining of tumour tissues. **B** LMVD bar diagram of each group. Scale bar 100 nm

## References

- Azzali G (2003) Transendothelial transport and migration in vessels of the apparatus lymphaticus periphericus absorbens (ALPA). *Int Rev Cytol* 230:42–89
- Balaji S, Mohamed Subarkhan MK, Ramesh R, Wang H, Semeril D (2020) Synthesis and structure of arene Ru(II) N $\wedge$ O-chelating complexes: in vitro cytotoxicity and cancer cell death mechanism. *Organometallics* 39:1366–1375. <https://doi.org/10.1021/acs.organomet.0c00092>
- Berg D (2006) In vivo detection of iron and neuromelanin by transcranial sonography—a new approach for early detection of substantia nigra damage. *J Neural Transm* 113:775–780
- Chen Y, Liang Y, Jiang P, Li F, Yu B, Yan F (2019) Lipid/PLGA hybrid microbubbles as a versatile platform for noninvasive image-guided targeted drug delivery. *ACS Appl Mater Interfaces* 11:41842–41852
- Chen M, Lv Z, Qian F, Wang Y, Xing X, Zhou K, Wang J, Huang S, Han S-T, Zhou Y (2021) Phototunable memories and reconfigurable logic applications based on natural melanin. *J Mater Chem C* 9:3569–3577. <https://doi.org/10.1039/D1TC00052G>
- Danafar H (2018) Preparation and characterization of PCL-PEG-PCL copolymeric nanoparticles as polymersomes for delivery hydrophilic drugs. *Iran J Pharm Sci* 14:21–32
- Devulapally R, Lee T, Barghava-Shah A, Sekar TV, Foygel K, Bachawal SV, Willmann JK, Paulmurugan R (2018) Ultrasound-guided delivery of thymidine kinase–nitroreductase dual therapeutic genes by PEGylated-PLGA/PEI nanoparticles for enhanced triple negative breast cancer therapy. *Nanomedicine* 13:1051–1066
- Di Salvo DN (2001) A new view of the neonatal brain: clinical utility of supplemental neurologic US imaging windows. *Radiographics* 21:943–955
- Di Ianni T, Bose RJC, Sukumar UK, Bachawal S, Wang H, Telichko A, Herickhoff C, Robinson E, Baker S, Vilches-Moure JG (2019) Ultrasound/microbubble-mediated targeted delivery of anticancer microRNA-loaded nanoparticles to deep tissues in pigs. *J Control Release* 309:1–10
- Ding Y, Li Z, Jaklenc A, Hu Q (2021) Vaccine delivery systems toward lymph nodes. *Adv Drug Deliv Rev* 179:113914
- Eide PK, Vatnehol SAS, Emblem KE, Ringstad G (2018) Magnetic resonance imaging provides evidence of glymphatic drainage from human brain to cervical lymph nodes. *Sci Rep* 8:1–10
- Ferrara KW, Merritt CRB, Burns PN, Foster FS, Mattrey RF, Wickline SA (2000) Evaluation of tumor angiogenesis with US: imaging, Doppler, and contrast agents. *Acad Radiol* 7:824–839
- Gong Y, Xing X, Wang Y, Lv Z, Zhou Y, Han S-T (2021) Emerging MXenes for functional memories. *Small Sci* 1:2100006. <https://doi.org/10.1002/smssc.202100006>
- Huang S, Ziegler CGK, Austin J, Mannoun N, Vukovic M, Ordovas-Montanes J, Shalek AK, von Andrian UH (2021) Lymph nodes are innervated by a unique population of sensory neurons with immunomodulatory potential. *Cell* 184:441–459
- Jung SJ (2012) Protocol development for observation of the primo vascular system in lymphatic system. *J Acupunct Meridian Stud* 5:234–240
- Kato T, Prevo R, Steers G, Roberts H, Leek RD, Kimura T, Kameoka S, Nishikawa T, Kobayashi M, Jackson DG (2005) A quantitative analysis of lymphatic vessels in human breast cancer, based on LYVE-1 immunoreactivity. *Br J Cancer* 93:1168–1174
- Koukourakis MI, Giatromanolaki A, Sivridis E, Simopoulos C, Gatter KC, Harris AL, Jackson DG (2005) LYVE-1 immunohistochemical assessment of lymphangiogenesis in endometrial and lung cancer. *J Clin Pathol* 58:202–206
- Kumar SU, Telichko AV, Wang H, Hyun D, Johnson EG, Kent MS, Rebhun RB, Dahl JJ, Culp WTN, Paulmurugan R (2020) Acoustically driven microbubbles enable targeted delivery of microRNA-loaded nanoparticles to spontaneous hepatocellular neoplasia in canines. *Adv Ther* 3:2000120
- Lee C, Jeong S, Jang C, Bae H, Kim YH, Park I, Kim SK, Koh GY (2019) Tumor metastasis to lymph nodes requires YAP-dependent metabolic adaptation. *Science* 363:644–649
- Li Y, Wu M, Zhang N, Tang C, Jiang P, Liu X, Yan F, Zheng H (2018) Mechanisms of enhanced antiangiogenic efficacy of polysorbate 80-modified paclitaxel-loaded PLGA nanoparticles by focused ultrasound. *J Cell Mol Med* 22:4171–4182
- Liu Z, Lammers T, Ehling J, Fokong S, Bornemann J, Kiessling F, Gätjens J (2011) Iron oxide nanoparticle-containing microbubble composites as contrast agents for MR and ultrasound dual-modality imaging. *Biomaterials* 32:6155–6163
- Liu J, Li H-J, Luo Y-L, Xu C-F, Du X-J, Du J-Z, Wang J (2019a) Enhanced primary tumor penetration facilitates nanoparticle draining into lymph nodes after systemic injection for tumor metastasis inhibition. *ACS Nano* 13:8648–8658

- Liu H, Ren F, Zhou X, Ma C, Wang T, Zhang H, Sun Q, Li Z (2019b) Ultra-sensitive detection and inhibition of the metastasis of breast cancer cells to adjacent lymph nodes and distant organs by using long-persistent luminescence nanoparticles. *Anal Chem* 91:15064–15072
- Lv Z, Chen M, Qian F, Roy VAL, Ye W, She D, Wang Y, Xu Z-X, Zhou Y, Han S-T (2019) Mimicking neuroplasticity in a hybrid biopolymer transistor by dual modes modulation. *Adv Funct Mater* 29:1902374. <https://doi.org/10.1002/adfm.201902374>
- Lv Z, Wang Y, Chen J, Wang J, Zhou Y, Han S-T (2020) Semiconductor quantum dots for memories and neuromorphic computing systems. *Chem Rev* 120:3941–4006. <https://doi.org/10.1021/acs.chemrev.9b00730>
- Mohamed Kasim MS, Sundar S, Rengan R (2018) Synthesis and structure of new binuclear ruthenium(II) arene benzil bis(benzoylhydrazone) complexes: investigation on antiproliferative activity and apoptosis induction. *Inorg Chem Front* 5:585–596. <https://doi.org/10.1039/C7Q100761B>
- Mohamed Subarkhan MK, Ramesh R, Liu Y (2016) Synthesis and molecular structure of arene ruthenium(II) benzhydrazone complexes: impact of substitution at the chelating ligand and arene moiety on antiproliferative activity. *New J Chem*. <https://doi.org/10.1039/c6nj01936f>
- Mohan N, Mohamed Subarkhan MK, Ramesh R (2018) Synthesis, antiproliferative activity and apoptosis-promoting effects of arene ruthenium(II) complexes with N, O chelating ligands. *J Organomet Chem*. <https://doi.org/10.1016/j.jorganchem.2018.01.022>
- Najibi AJ, Mooney DJ (2020) Cell and tissue engineering in lymph nodes for cancer immunotherapy. *Adv Drug Deliv Rev* 161–162:42–62
- Ohtani O, Ohtani Y (2008) Structure and function of rat lymph nodes. *Arch Histol Cytol* 71:69–76
- Prat F, Centarti M, Sibille A, El Fadil FA, Henry L, Chapelon J, Cathignol D (1995) Extracorporeal high-intensity focused ultrasound for VX2 liver tumors in the rabbit. *Hepatology* 21:832–836
- Price RJ (2018) Targeted delivery of controlled release nanoparticles to brain tumors using contrast agent microbubbles and high-intensity focused ultrasound
- Sanz-Ortega L, Rojas JM, Marcos A, Portilla Y, Stein JV, Barber DF (2019) T cells loaded with magnetic nanoparticles are retained in peripheral lymph nodes by the application of a magnetic field. *J Nanobiotechnol* 17:1–20
- Sathiyakamatchi T, Mohamed Subarkhan MK, Ramesh R, Wang H, Malecki JG (2020) Investigation into antiproliferative activity and apoptosis mechanism of new arene Ru(II) carbazole-based hydrazone complexes. *Dalt Trans* 49:11385–11395. <https://doi.org/10.1039/D0DT01476A>
- Schreuder A, Jacobs C, Scholten ET, van Ginneken B, Schaefer-Prokop CM, Prokop M (2020) Typical CT features of intrapulmonary lymph nodes: a review. *Radiol Cardiothorac Imaging* 2:e190159
- Schudel A, Chapman AP, Yau M-K, Higginson CJ, Francis DM, Manspeaker MP, Avecilla ARC, Rohner NA, Finn MG, Thomas SN (2020) Programmable multistage drug delivery to lymph nodes. *Nat Nanotechnol* 15:491–499
- Shen X, Li T, Xie X, Feng Y, Chen Z, Yang H, Wu C, Deng S, Liu Y (2020) PLGA-based drug delivery systems for remotely triggered cancer therapeutic and diagnostic applications. *Front Bioeng Biotechnol* 8:381
- Shi H, Yan R, Wu L, Sun Y, Liu S, Zhou Z, He J, Ye D (2018) Tumor-targeting CuS nanoparticles for multimodal imaging and guided photothermal therapy of lymph node metastasis. *Acta Biomater* 72:256–265
- Som PM, Francois M (2017) The current concepts of the embryology of the lymphatic system. *Neurographics* 7:129–150
- Sonamuthu J, Cai Y, Liu H, Kasim MSM, Vasanthakumar VR, Pandi B, Wang H, Yao J (2020) MMP-9 responsive dipeptide-templated natural protein hydrogel-based wound dressings for accelerated healing action of infected diabetic wound. *Int J Biol Macromol* 153:1058–1069. <https://doi.org/10.1016/j.ijbiomac.2019.10.236>
- Steiner DF, MacDonald R, Liu Y, Truszkowski P, Hipp JD, Gammage C, Thng F, Peng L, Stumpe MC (2018) Impact of deep learning assistance on the histopathologic review of lymph nodes for metastatic breast cancer. *Am J Surg Pathol* 42:1636
- Subarkhan MKM, Ramesh R (2016) Ruthenium(II) arene complexes containing benzhydrazone ligands: Synthesis, structure and antiproliferative activity. *Inorg Chem Front* 3:1245–1255. <https://doi.org/10.1039/c6qi00197a>
- Wang X, Niu D, Li P, Wu Q, Bo X, Liu B, Bao S, Su T, Xu H, Wang Q (2015) Dual-enzyme-loaded multifunctional hybrid nanogel system for pathological responsive ultrasound imaging and T2-weighted magnetic resonance imaging. *ACS Nano* 9:5646–5656
- Wang L, Chen S, Zhu Y, Zhang M, Tang S, Li J, Pei W, Huang B, Niu C (2018) Triple-modal imaging-guided chemo-photothermal synergistic therapy for breast cancer with magnetically targeted phase-shifted nanoparticles. *ACS Appl Mater Interfaces* 10:42102–42114
- Willmann JK, Paulmurugan R, Chen K, Gheysens O, Rodriguez-Porcel M, Lutz AM, Chen IY, Chen X, Gambhir SS (2008) US imaging of tumor angiogenesis with microbubbles targeted to vascular endothelial growth factor receptor type 2 in mice. *Radiology* 246:508–518
- Witte MH, Bernas MJ, Martin CP, Witte CL (2001) Lymphangiogenesis and lymphangiodysplasia: from molecular to clinical lymphology. *Microsc Res Tech* 55:122–145
- Xin Y, Qi Q, Mao Z, Zhan X (2017) PLGA nanoparticles introduction into mitoxantrone-loaded ultrasound-responsive liposomes: *in vitro* and *in vivo* investigations. *Int J Pharm* 528:47–54
- Xu Y, Niu C, An S, Tang S, Xiao P, Peng Q, Wang L (2017) Thermal-sensitive magnetic nanoparticles for dual-modal tumor imaging and therapy. *RSC Adv* 7:40791–40802
- Yu X, Dai Y, Zhao Y, Qi S, Liu L, Lu L, Luo Q, Zhang Z (2020) Melittin-lipid nanoparticles target to lymph nodes and elicit a systemic anti-tumor immune response. *Nat Commun* 11:1–14
- Zaki NM, Hafez MM (2012) Enhanced antibacterial effect of ceftriaxone sodium-loaded chitosan nanoparticles against intracellular *Salmonella typhimurium*. *Aaps Pharmscitech* 13:411–421
- Zhang C, Li X, Zhang Z, Lei S, Fan P, Xiao Q (2019a) The potential role of carbon nanoparticles-assisted biopsy for sentinel lymph nodes of incidental thyroid carcinoma. *Gland Surg* 8:370
- Zhang Y, Yong L, Luo Y, Ding X, Xu D, Gao X, Yan S, Wang Q, Luo J, Pu D (2019b) Enhancement of HIFU ablation by sonosensitizer-loading liquid fluorocarbon nanoparticles with pre-targeting in a mouse model. *Sci Rep* 9:1–18
- Zhu J (2020) Imaging lymphatic system using high frame rate contrast enhanced and super-resolution ultrasound: *in vitro*, *in vivo* and clinical study
- Zhuang J, Fan K, Gao L, Lu D, Feng J, Yang D, Gu N, Zhang Y, Liang M, Yan X (2012) Ex vivo detection of iron oxide magnetic nanoparticles in mice using their intrinsic peroxidase-mimicking activity. *Mol Pharm* 9:1983–1989
- Zukancic D, Suys EJA, Pilkington EH, Algarni A, Al-Wassiti H, Truong NP (2020) The importance of poly (ethylene glycol) and lipid structure in targeted gene delivery to lymph nodes by lipid nanoparticles. *Pharmaceutics* 12:1068

**Publisher's Note** Springer Nature remains neutral with regard to jurisdictional claims in published maps and institutional affiliations.